ACS Partner Journal

Journal of the American Society for Mass Spectrometry

pubs.acs.org/jasms

Research Article

High-Resolution Ion Microscope Imaging over Wide Mass Ranges Using Electrodynamic Postextraction Differential Acceleration

Ang Guo, Robert J. Burleigh, Natasha Smith, Mark Brouard,* and Michael Burt*

Cite This: *J. Am. Soc. Mass Spectrom.* 2020, 31, 1903−1909

Read Online

ACCESS | Metrics & More | Article Recommendations

ABSTRACT: A time-dependent postextraction differential acceleration (PEDA) potential was used to temporally focus increasingly heavy ions in a stigmatic imaging mass spectrometer, allowing them to be imaged with high mass and spatial resolutions over a broad mass-to-charge (m/z) range. By applying a linearly rising potential to the ion extraction electrode, sequential m/z ratios were subjected to a changing electric field, allowing their foci to coincide at the detector. Using this approach, at least 75% of the maximum mass resolution was obtained over a 300−600 Da range when the ion microscope was focused around 450 Da, representing more than a 10-fold increase over the conventional single-field PEDA method.

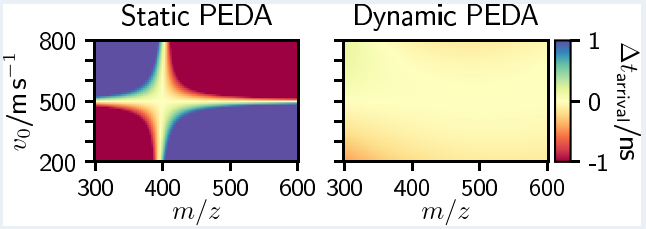

INTRODUCTION

High-throughput imaging of spatially localized chemical distributions plays a central role in many disciplines. Pathology and drug discovery particularly benefit from the rapid identification of biomarkers or proteins in assays and tissues. These and similar experiments often employ mass spectrometry imaging (MSI) to record and assign mass spectra to defined spatial coordinates on a sample.[1−4] MSI provides a wealth of information: results can be integrated over mass to extract images of distinct compounds or over position to compare mass spectra from different regions of a sample.

MSI is conventionally performed by raster scanning a focused ion or laser beam across a surface to acquire mass spectra at different coordinates. Ion images are constructed pixel by pixel, with spatial resolutions defined by the spot size of the microprobe, which can be as narrow as 50 nm or 1 μm when using secondary ion mass spectrometry (SIMS) or matrix-assisted laser desorption ionization (MALDI), respectively.[5,6] The acquisition time of an ion image is therefore inversely proportional to the square of the desired spatial resolution, meaning that the latter comes at the expense of throughput.

Stigmatic ion microscope imaging is an alternative MSI technique that decouples acquisition time from spatial resolution by using a defocused ionization source to simultaneously ionize relatively larger sample areas, typically 0.05 mm^2 to 1 cm^2. An image of the sample plane is then electrostatically projected onto a position-sensitive detector at the end of a time-of-flight mass analyzer.[7−11] This allows ion images to be recorded sequentially for any mass-resolved compounds in the sample using multimass imaging sensors.[12−22] In this approach, the spatial resolution depends on the distribution of initial velocities of the ions emitted from the surface as well as the strength of the extraction field. In typical instruments, the achievable spatial resolution is 1−10 μm.

Ion optical focusing with fixed voltages optimizes the mass and spatial resolutions for a specific mass-to-charge ratio m/z, with the consequence that both, particularly the former, decrease at higher or lower m/z. As in other time-of-flight measurements, the mass resolution also depends on the distribution of initial ion velocities along the time-of-flight axis. Introducing a time lag between ion generation and the onset of the extraction field corrects for this by allowing the ions to move to new initial positions before acceleration, which focuses their spread of arrival times at the detector.[23] Delayed extraction techniques of this kind are used for energy focusing both parallel and orthogonal to ion beams but necessarily sacrifice the initial spatial information of the ions, which limits their value for microscope MSI.[24] In other words, it is crucial to detect where an ion hits in addition to when. To resolve this, a postextraction differential acceleration (PEDA) technique has been developed to retain high mass resolution through energy focusing, without compromising the achievable spatial resolution.[25]

Received: May 8, 2020
Revised: July 4, 2020
Accepted: July 31, 2020
Published: July 31, 2020

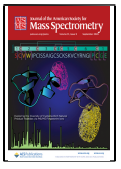

https://dx.doi.org/10.1021/jasms.0c00167
J. Am. Soc. Mass Spectrom. 2020, 31, 1903−1909

The PEDA technique immediately extracts surface ions following ionization to retain their spatial information and corrects for their initial velocity dispersion by raising the potential of the extraction electrode after the ions have passed through it. In this way, ions with slower initial velocities gain more kinetic energy from the voltage pulse than faster ions, creating a temporal focus point that can be superimposed on the detector to improve the mass resolution. Acceleration fields of this type are frequently used in mass spectrometry for energy focusing, for example in "LIFT" cells.[26] In the original PEDA configuration, the effective mass range is centered around a single m/z focused by the pulsed acceleration field.[25] Using this method, we showed that the mass range over which the mass resolution of our ion microscope reached at least half that of the focused m/z (410 Da) was just ~8% of the 300 Da range that could simultaneously be spatially resolved.[27,28]

In order to apply the benefits of PEDA over wider mass ranges, multiple m/z must be focused during an experiment. For example, the mass-resolved range of the above experiment can be extended to cover ~20% of the spatially resolved window using the double-field PEDA method, where the acceleration region is divided in two by an electrode that is raised to a higher potential at the same time as the extraction electrode.[28] The potentials of the two electrodes were set to create a cusp in the potential energy surface between the two acceleration regions, such that heavier ions in the "early" region achieved temporal overlap at the same drift distance as lighter ions in the "late" region. This approach could in principle be extended to a many-field method using additional electrodes to focus broader mass ranges.

This paper instead presents a more robust PEDA technique that electrodynamically adjusts the m/z focused during an experiment by applying a time-dependent voltage pulse to the extraction electrode after a set delay. The concept parallels the use of dynamic acceleration fields for m/z-correlated energy focusing following delayed extraction but retains the stigmatic imaging ability of the mass spectrometer.[29] Electrodynamic PEDA results in increasingly heavy ions being sequentially focused as they pass through the ion microscope, broadening the mass range that can be mass-resolved by an order of magnitude (expanding it to 100% of the spatially resolved 300 Da mass range described above). Every imageable compound can therefore be acquired with high mass resolution, facilitating multimass and high-resolution stigmatic particle imaging.

THEORY

PEDA narrows the time-of-flight spread observed when isobaric ions are emitted from a surface with a distribution of initial velocities. The technique is illustrated in Figure 1 and is applied by raising the potential of an extraction electrode, placed parallel to the surface, after the ions have passed through it. In this way, the spatial information of the ion packet is retained due to the electric field in the extraction region, while the mass resolution is increased by the differential acceleration and energy focusing imparted by the voltage pulse. Ions with slower initial velocities will be closer to the extraction electrode when the pulse is applied and accelerate to overlap with faster ions, creating a temporal focus point.

When the initial velocities of the generated ions are independent of mass, which is often the case in MALDI imaging experiments where they tend toward the average velocity of the ejected matrix ions,[30−32] then heavier m/z will exhibit wider time-of-flight distributions than lighter ions. This will in practice remain true even when the initial velocities are mass-dependent, as their relative contributions to the final velocities will still be much larger for heavier m/z. The PEDA pulse voltage must therefore be chosen to focus a particular m/z, with heavier ions requiring more acceleration to reach a temporal focus.

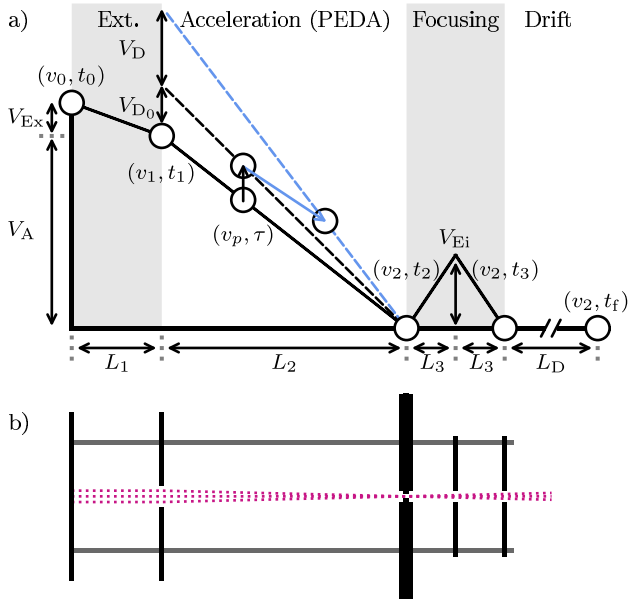

Figure 1. (a) Electrode potential energy surface (solid black line) of an ion microscope along its time-of-flight axis. In single-field PEDA (dashed black line), the extractor potential is raised by V_{D_0} at time τ so that ions (white circles) of a particular m/z are focused when they arrive at the detector plane at time t_f. Electrodynamic PEDA sequentially focuses additional m/z by continuing to raise the extractor potential as a function of time to a maximum V_D (blue dashed line). These ions are swept through different electric field strengths, as represented by the blue arrow. Additional details are provided in the Simulations section. (b) A generalized schematic of the corresponding ion optics, demonstrating stigmatic imaging (dotted violet lines) of a sample embedded in the repeller electrode. The image plane magnification depends on the distance between the ion crossover point and the detector.

Electrodynamic PEDA applies the benefits of single-field PEDA over a wider mass range by continuously raising the potential of the extraction electrode, such that different m/z are sequentially focused as they pass through the acceleration region. For a time-of-flight imaging mass spectrometer operating in a Wiley−McLaren configuration, the ideal pulse shape should be a quadratic rise, as the time a particular ion spends in the extraction and acceleration regions is proportional to $\sqrt{m/z}$.[23] In the experiments reported here, a linear pulse is used instead. Taylor's theorem demonstrates this will be approximately valid over 300−600 Da when the mass spectrometer is optimized to record ion images around 450 Da. This approach also circumvents the technical challenge of developing a fast-rising quadratic pulse.

SIMULATIONS

The ion optical system described in Figure 1 creates separate ion extraction and differential acceleration regions. In the former, an ion generated from the sample plate at $x = 0$ with mass m, charge q, and velocity v_0 is accelerated through a

https://dx.doi.org/10.1021/jasms.0c00167
J. Am. Soc. Mass Spectrom. 2020, 31, 1903−1909

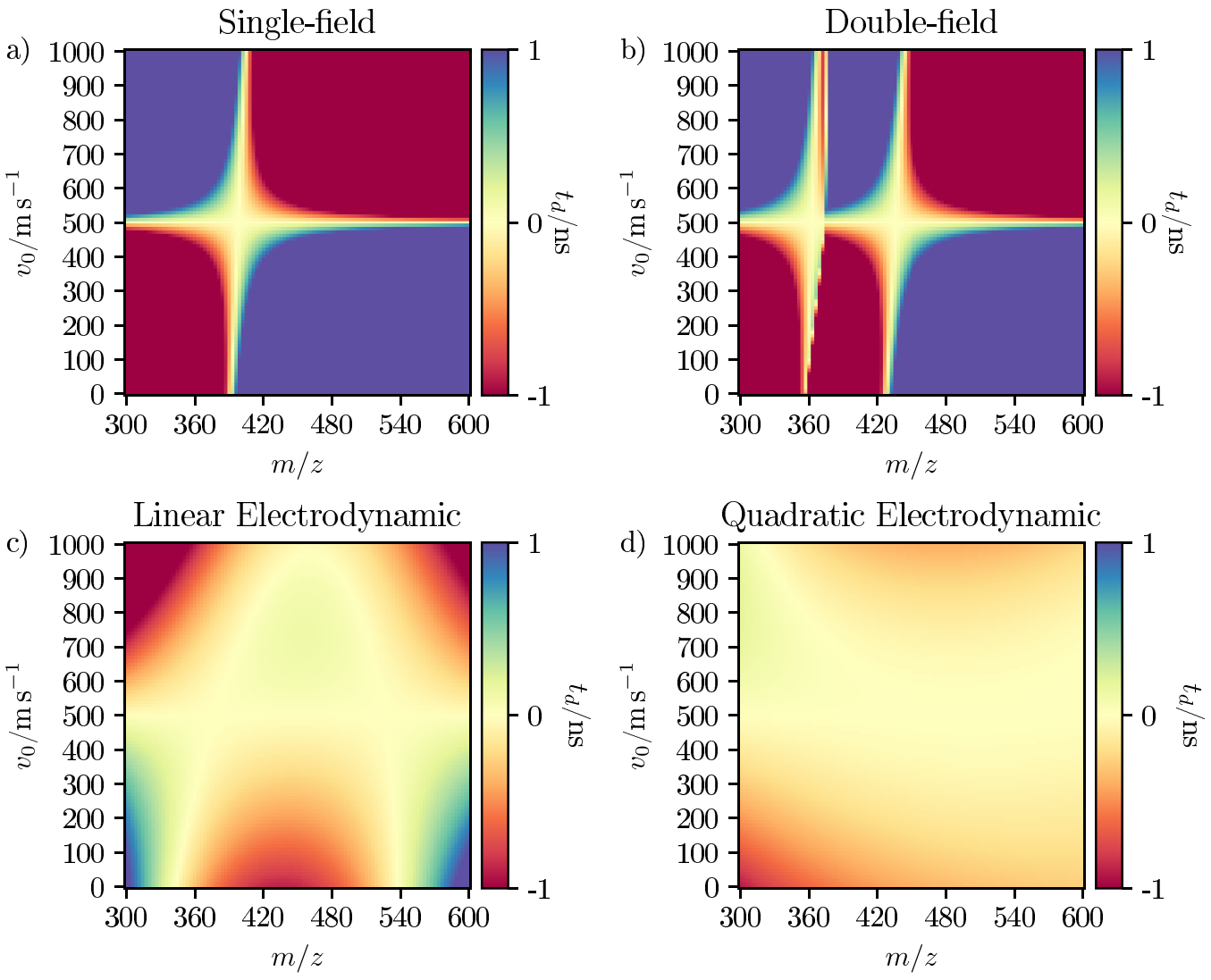

Figure 2. Time-of-flight difference (t_d) maps calculated for ions focused by (a) single-field PEDA, (b) double-field PEDA, (c) linear electrodynamic PEDA, and (d) quadratic electrodynamic PEDA. The 300−600 Da window covers the range over which the ion microscope can experimentally record spatially focused images, when optimized using the parameters listed in the text. Each map is scaled between ±1 ns. Using this metric, the linear and quadratic electrodynamic pulses focus 96 and 100% of the 300 Da window, considerably improving upon the usable range of the single- and double-field methods.

potential difference V_{Ex} toward the extraction electrode at $x = L_1$. At this point, its velocity v_1 and flight time t_1 are

$$v_1 = \sqrt{\frac{2}{m}\left(\frac{mv_0^2}{2} + qV_{Ex}\right)} \tag{1}$$

$$t_1 = \frac{mv_0L_1}{qV_{Ex}}\left(-1 + \sqrt{1 + \frac{2qV_{Ex}}{mv_0^2}}\right) \tag{2}$$

The ion then enters the acceleration region, where it passes through a potential difference V_A as it travels toward the grounded entrance of an einzel lens at $L_1 + L_2$. After a set time τ, the ion is located within this domain at $L_1 + \Delta x$ and has a velocity v_p

$$\Delta x = v_1(\tau - t_1) + \frac{qV_A}{2mL_2}(\tau - t_1)^2 \tag{3}$$

$$v_p = \sqrt{\frac{2}{m}\left[\frac{1}{2}mv_0^2 + q\left(V_{Ex} + V_A\frac{\Delta x}{L_2}\right)\right]} \tag{4}$$

At τ, electrodynamic PEDA can be initiated by applying a time-dependent potential $V_D(t, k)$ to the extractor. In the following experiments, the electrode is raised by a PEDA step potential V_{D_0} and continuously increased until it reaches a maximum V_D. The rate constant k associated with this change is defined as the inverse time constant of the resistor−capacitor circuit that creates the pulse, such that

$$V_D(t, k) = V_{D_0} + V_D(1 - e^{-k(t-\tau)}) \tag{5}$$

Ions in the acceleration region are therefore subjected to shifting PEDA conditions, which initially focus a particular m/z at V_{D_0} and gradually focus larger m/z as the electric field strengthens. $V_D(t, k)$ will effectively be linear at times close to τ for small k, as required. Governed by this environment, a given

https://dx.doi.org/10.1021/jasms.0c00167
J. Am. Soc. Mass Spectrom. 2020, 31, 1903−1909

ion will leave the acceleration region with a velocity v_2 after a flight time t_2

$$v_2 = v_p + \frac{q}{mL_2}\int_{\tau}^{t_2} V_A + V_D(t, k)dt = v_p + \frac{q}{mL_2}\left[V\Delta t - \frac{V_D}{k}(1 - e^{-k\Delta t})\right] \quad (6)$$

In the above equation, the total acceleration potential $V = V_A + V_{D_0} + V_D$ and PEDA flight time $\Delta t = t_2 - \tau$ were defined for convenience. Integrating v_2 with respect to time demonstrates that t_2 satisfies the following equation, which can be solved numerically or through a Taylor expansion to determine Δt and hence v_2

$$L_2 - \Delta x = \left(v_p - \frac{q}{mL_2}\right)\Delta t + \frac{q}{mL_2}\left[\frac{V(\Delta t)^2}{2} + \frac{V_D^2}{k^2}(1 - e^{-k\Delta t})\right] \quad (7)$$

After leaving the acceleration region, the ions travel through a conventional three-electrode einzel lens and field-free drift distance L_D before impacting the detector. The central potential of the lens is V_{Ei}, and each electrode is separated by a length L_3. The ions exit the einzel lens after a flight time t_3 with the same velocity v_2 that they entered with. As a consequence, the total time-of-flight t_f for a particular ion is

$$t_3 = t_2 + 2\frac{mv_2L_3}{qV_{Ei}}\left(1 + \sqrt{\frac{1 - 2qV_{Ei}}{mv_2^2}}\right) \quad (8)$$

$$t_f = t_3 + \frac{L_D}{v_2} \quad (9)$$

The PEDA pulse ensures that, for a given m/z, ions with slower initial velocities leave the einzel lens with a larger v_2 than ions with faster initial velocities. An m/z packet will therefore reach a temporal focus within the field-free region, and this position can be tuned to correspond with a position-sensitive detector. Electrodynamic PEDA should additionally allow larger m/z to be consecutively focused to the same point. As the instrument parameters and potentials are fixed for a given experiment, the performance of electrodynamic PEDA can be assessed by calculating the expected times-of-flight for different m/z across a range of initial velocities and comparing them to flight times determined using an average initial velocity $\overline{v_0}$. The resulting time-of-flight difference t_d provides a measure of the expected energy focusing and time-of-flight resolution at the detector. A smaller t_d corresponds to higher mass resolution and vice versa.

$$t_d = t_f\left(v_0, \frac{m}{z}\right) - t_f\left(\overline{v_0}, \frac{m}{z}\right) \quad (10)$$

Figure 2 compares the calculated time-of-flight differences of four PEDA variants: single-field, double-field, linear electrodynamic, and quadratic electrodynamic (Figure 2a–d, respectively). Each was determined relative to an average initial ion velocity of 500 m s^{-1} over v_0 = 0–1000 m s^{-1} and m/z = 300–600 Da. The chosen instrument parameters were L_1 = 1.45 cm, L_2 = 3.95 cm, L_3 = 0.79 cm, L_D = 91.02 cm, V_{Ex} = 400 V, V_A = 4550 V, V_{Ei} = 1728 V, and τ = 2.59 μs. Figure 2a,b were modeled using the calculations developed by Aoki and Guo.[25,28] The extractor step potential was 930 V for single-field PEDA and 920 V for the double-field case. The second PEDA electrode of the latter was situated at the midpoint of the acceleration region and raised by 410 V. For Figure 2c, τ was changed to 2.67 μs to optimize the approximately linear electrodynamic PEDA pulse $V_D(t, k)$ over the 300–600 Da window. This was modeled using V_{D_0} = 544 V, V_D = 2590 V, and $k = 2.3 \times 10^5$ s^{-1}. The quadratic electrodynamic PEDA pulse used for Figure 2d was shaped using

$$V_D(t) = V_{D_0} + a(\Delta t)^2 + b\Delta t \quad (11)$$

The constants a, b, and V_{D_0} were set to 1.814×10^{13} V s^{-2}, 4.990×10^8 V s^{-1}, and 580 V following their optimization by a genetic algorithm that minimized t_d over the range of v_0 and m/z considered. For consistency with Figure 2a–c, only V_{D_0}, τ, a, and b were allowed to vary. Substituting $V_D(t)$ for $V_D(t, k)$ in eq 6 allows Δt to be determined following integration in a similar manner to the linear electrodynamic case.

The simulations in Figure 2 are scaled to ±1 ns. This corresponds to a resolution of 7500 for an ion flight time of 30 μs, which is typical for the parameters used. Figure 2a,b demonstrates that single- and double-field PEDA meet or exceed this resolution over relatively small ranges, just 15 and 22% of the 300 Da window shown. The linear electrodynamic pulse in Figure 2c, which can be thought of as a many-field adaptation of the double-field method, improves this result to 96%, indicating that it will significantly broaden the overall mass range that can be experimentally imaged with high mass resolution. As expected, the quadratic pulse modeled in Figure 2d provides even better performance, focusing the entire window to at least ±1 ns. This behavior holds even when the window is extended to 900 Da, whereas the focusing ability of the linear pulse decreases sharply after 600 Da.

The linear electrodynamic pulse can only match quadratic behavior at two points. It should therefore create two temporally focused maxima with reduced performance in between. This effect can be seen in Figure 2c, where the two focused regions around 345 and 540 Da are connected by a curve of focused ions with faster than average initial velocities. This curve occurs because, between these two focal points, the linearly rising pulse overcompensates for the kinetic energy needed to create a temporal focus at the detector. Relatively fast ions in this range will spend less time in the PEDA differential acceleration region and counteract this effect.

Figure 3 depicts the time-dependent PEDA potentials $V_D(t, k)$ (blue dotted line) and $V_D(t)$ (black solid line) used for Figure 2c,d. A linear fit of the latter (gray dashed line) demonstrates that each pulse is essentially linear between its onset and the time at which ions heavier than 600 Da exit the acceleration region (blue shaded area). The applied pulse $V_D(t, k)$ is therefore expected to exhibit similar performance to the quadratic pulse $V_D(t)$ over a 300 Da range, matching the window over which ion images can be recorded with high spatial resolutions experimentally. It is worth noting that due to the 0.08 μs difference in τ, $V_D(t, k)$ does not cross $V_D(t)$ as described above. This is a consequence of positioning the focal points of the linear pulse near the center of the simulated mass range in Figure 2c, whereas the optimized quadratic pulse begins to focus ions at lower m/z.

METHODS

Electrodynamic PEDA was tested using a time-of-flight microscope imaging mass spectrometer. The instrument has

https://dx.doi.org/10.1021/jasms.0c00167
J. Am. Soc. Mass Spectrom. 2020, 31, 1903–1909

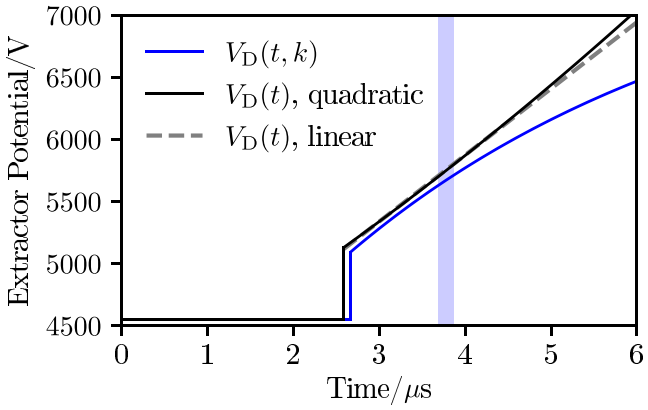

Figure 3. Time-dependent PEDA potentials $V_D(t, k)$ (blue solid line) and $V_D(t)$ (black solid line) used to simulate Figure 2c,d. These are virtually linear from their onsets until the time at which ions are no longer spatially focused by the mass spectrometer (blue shaded area) and are similar to a linear fit of $V_D(t)$ (gray dashed line).

an adaptable chamber that can be configured as an approximately linear ion microscope or as a two-stage system where the temporal PEDA focus is used as a pseudosource for a reflectron.[33] The linear configuration was used here to better compare the data with previous experiments, which shared the same ion optical system but a shorter drift distance.[28] The ion optical dimensions are therefore the same as those used for Figures 1b and 2 but with $L_D \simeq 240$ cm. The instrument is also not perfectly linear; the ions were deflected by 3° toward the detector using two parallel plate electrodes held at ±157.2 V and placed 72.1 cm from the exit of the einzel lens. Despite these differences, the optimal electrode potentials and pulse timing were similar to those used in the simulations, with V_{Ex} = 439 V, V_A = 4561 V, V_{Ei} = 1950 V, V_{D_0} = 262 V, V_D = 2877 V, and τ = 2.60 μs. The most noticeable discrepancy is the drop in the PEDA step voltage, which is simply a consequence of the longer flight distance. The shape and magnitude of the PEDA pulse $V_D(t, k)$ were experimentally verified, as described elsewhere.[34] Using the above settings, SIMION 8.1 predicts the mass and spatial resolutions of the instrument to be about 3800 $m/\Delta m$ (under single-field PEDA conditions) and 20 μm, respectively.

The mass and spatial resolutions established by electrodynamic PEDA were determined as functions of m/z by recording mass spectra and ion images for five dyes (Auramine O, Exalite 404, Kiton Red, Rhodamine B, and Rhodamine 6G chloride). Each sample was electrosprayed through a nickel mesh onto conductive 25 × 25 mm indium tin oxide plates to produce grids with 38.1 μm gaps and 102 μm pitches. These were individually placed into a recess in the repeller electrode and desorbed by 9 mJ pulses delivered at 10 Hz by a 355 nm Nd:YAG laser (Continuum Powerlight 8010) focused to cover 10 × 10 mm of the sample. The resulting ion images were then electrostatically transferred through the optics described in Figure 1 and projected onto a position-sensitive detector comprising dual-stack microchannel plates and an Exalite 404 screen. Mass spectra and ion images were recorded from the ensuing flashes of light by a photomultiplier tube and by an intensified 768 × 568 pixel CCD camera (Photonic Science) gated on the m/z of interest.

RESULTS

Mass Resolution. Figure 4 illustrates the mass resolution dependence of the electrodynamic PEDA method on m/z,

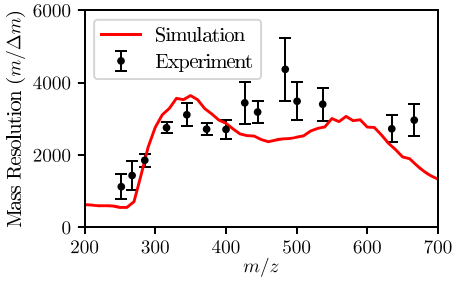

Figure 4. Mass resolution dependence on m/z of electrodynamic PEDA. The experimental resolution (black circles) covers the 300–600 Da imaging range of the ion microscope and is comparable to the simulated trend (red line) determined using SIMION 8.1.

subject to the experimentally applied pulse $V_D(t, k)$. SIMION 8.1 (red trace) predicts two focused mass ranges centered at 350 and 570 Da using these conditions, with maxima at 3600 and 3000, respectively. The former compares well with the mass resolution of 3800 simulated when using single-field PEDA, demonstrating that sequentially focusing multiple m/z does not significantly reduce the attainable resolution of the instrument. The slight drop in performance between the two maxima can be attributed to the applied pulse, which can only approximate quadratic behavior at two points.

The measured mass resolutions of the dyes match the simulated trend and surpass it between the two maxima. They are also relatively insensitive to m/z over 300–600 Da. Electrodynamic PEDA therefore extends the mass range over which the mass resolution is at least half of its maximum obtainable value from 8% coverage of the spatially resolved window in the single-field PEDA case to 100%, when focused around similar m/z. Moreover, this approach significantly outperforms this metric. Each data point exceeds 2700 $m/\Delta m$, which corresponds to approximately 75% of the maximum predicted value.

In principle, the applicable mass range of this method could be broadened so long as the required PEDA focusing voltage remained approximately linear. Kovtoun and co-workers demonstrated this for m/z-correlated energy focusing following delayed extraction by carefully tuning their ion optical spacings L_1 and L_2.[29] However, as the applied pulse used here already covered the spatially resolved window, no additional ion optical adjustments were needed. The resolvable mass range can also be easily shifted to image different m/z by adjusting each electrode potential using a linear scaling factor, as described elsewhere.[28,35] The widths of the mass-resolved and spatially resolved windows will also change roughly in line with this factor, meaning that broader mass ranges can be imaged if the ion microscope is focused for heavier m/z. This approach provides flexibility, but it is worth noting that it is limited by the voltages that can safely be applied to the ion optics.

Spatial Resolution. PEDA was originally developed to enhance the mass resolution achievable through ion microscopy without compromising the spatial resolution. Figure 5a demonstrates that this property holds for electrodynamic PEDA as well, as the average recorded spatial resolution is 25 ± 3 μm between 300 and 600 Da. These results are consistent

https://dx.doi.org/10.1021/jasms.0c00167
J. Am. Soc. Mass Spectrom. 2020, 31, 1903–1909

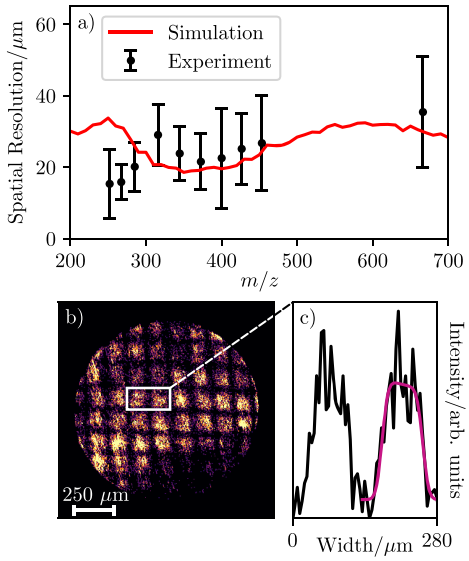

Figure 5. (a) The spatial resolution dependence on m/z of electrodynamic PEDA. The experimental resolution (black circles) is 25 ± 3 μm between 300 and 600 Da, matching the simulated trend (red line) obtained from SIMION 8.1 and demonstrating that this method preserves the stigmatic imaging condition. (b) For each m/z, the spatial resolution was determined by gating the CCD camera over the arrival times of interest to produce grid-patterned ion images. (c) The 20−80% intensity rises obtained from these images were then used to determine the Gaussian standard deviation σ and hence the spatial resolution. The ion image of the 371 Da Rhodamine B fragment is shown as an example. Fitting the right-hand peak (purple line) returns a spatial resolution of 15 μm. Repeating this calculation over each resolved grid yields an average spatial resolution of 22 ± 8 μm at this m/z.[36,37]

with the simulation (red trace) and with the expected resolution of the ion microscope with and without a PEDA pulse applied.[21,28,33]

The spatial resolution was determined independently for each recorded ion by gating the CCD camera over the m/z range of interest to produce images of the gridded dye samples, such as the one shown in Figure 5b. The spatial resolutions were then determined by averaging the 20−80% intensity rises (Figure 5c) of the grid patterns to determine the corresponding Gaussian standard deviations σ[36] and then dividing them by the image magnification M according to[37]

$$R_s = \frac{1.68\sigma}{M} \tag{12}$$

The image magnification was determined to be about 21.6 using the 140.1 μm pitch of the nickel mesh, which corresponds to an image diameter of ∼1.16 mm.

CONCLUSION

Electrodynamically adjusting a PEDA pulse enables stigmatic imaging with high mass and spatial resolutions over a wide m/z range. This is a direct improvement on the single-field method, which focuses one m/z and becomes less resolved at higher or lower values.[25] It is also a simpler alternative to the many-field PEDA approach that can be applied without modifying or adding new electrodes to an ion optical system.[28,34] Only the applied pulse to the extraction electrode is changed. In these experiments, an approximately linear potential rise was used. Over small m/z ranges, this pulse shape is comparable to the quadratic dependence expected for time-of-flight mass spectrometry.

Faster and more controllable electronics would enable even better performance over wider m/z ranges, as was demonstrated in Figure 2c,d. However, in this case, the linear pulse was able to achieve at least 75% of the maximum mass resolution over the 300−600 Da spatially resolved window, demonstrating that the quadratic pulse is not necessary if the ion microscope is focused around 450 Da. This metric compares favorably with the single- and double-field PEDA methods, which under comparable conditions only reached at least 75% of the maximum mass resolution over 6.6 and 8.2% of the same range, respectively.[28]

The capacity to image and mass resolve multiple m/z with high resolution suits the high-throughout capability of ion microscope imaging. Stigmatic imaging mass spectrometry with electrodynamic PEDA therefore offers an efficient approach to quickly extracting high-quality images and ion−ion correlations from complex or time-limited samples.

AUTHOR INFORMATION

Corresponding Authors

Mark Brouard − *The Chemistry Research Laboratory, Department of Chemistry, University of Oxford, Oxford OX1 3TA, United Kingdom;* orcid.org/0000-0003-3421-0850; Email: mark.brouard@chem.ox.ac.uk

Michael Burt − *The Chemistry Research Laboratory, Department of Chemistry, University of Oxford, Oxford OX1 3TA, United Kingdom;* orcid.org/0000-0002-7317-8649; Phone: +44 1865 275980; Email: michael.burt@chem.ox.ac.uk

Authors

Ang Guo − *The Chemistry Research Laboratory, Department of Chemistry, University of Oxford, Oxford OX1 3TA, United Kingdom*

Robert J. Burleigh − *The Chemistry Research Laboratory, Department of Chemistry, University of Oxford, Oxford OX1 3TA, United Kingdom*

Natasha Smith − *The Chemistry Research Laboratory, Department of Chemistry, University of Oxford, Oxford OX1 3TA, United Kingdom*

Complete contact information is available at: https://pubs.acs.org/10.1021/jasms.0c00167

Notes

The authors declare no competing financial interest.

ACKNOWLEDGMENTS

The authors gratefully acknowledge support from the UK EPSRC (M.Br. - EP/L005913/1; M.Bu. - EP/S028617/1). A.G. additionally thanks the China Scholarship Council (CSC) for funding. N.S. thanks the EPSRC and National Physical Laboratory for her iCASE studentship, and R.J.B. is thankful to Jesus College, Oxford, for its financial support.

REFERENCES

(1) McDonnell, L. A.; Heeren, R. M. A. Imaging mass spectrometry. *Mass Spectrom. Rev.* **2007**, *26*, 606−643.

(2) Nilsson, A.; Goodwin, R. J. A.; Shariatgorji, M.; Vallianatou, T.; Webborn, P. J. H.; Andrén, P. E. Mass spectrometry imaging in drug development. *Anal. Chem.* **2015**, *87*, 1437−1455.

(3) Boughton, B. A.; Thinagaran, D.; Sarabia, D.; Bacic, A.; Roessner, U. Mass spectrometry imaging for plant biology: a review. *Phytochem. Rev.* **2016**, *15*, 445−488.
(4) Swales, J. G.; Hamm, G.; Clench, M. R.; Goodwin, R. J. A. Mass spectrometry imaging and its application in pharmaceutical research and development: A concise review. *Int. J. Mass Spectrom.* **2019**, *437*, 99−112.
(5) Veryovkin, I. V.; Calaway, W. F.; Tripa, C. E.; Pellin, M. J. Mass spectrometry on the nanoscale with ion sputtering based techniques: what is feasible. *Nucl. Instrum. Methods Phys. Res., Sect. B* **2007**, *261*, 508−511.
(6) Koestler, M.; Kirsch, D.; Hester, A.; Leisner, A.; Guenther, S.; Spengler, B. A high-resolution scanning microprobe matrix-assisted laser desorption/ionization ion source for imaging analysis on an ion trap/Fourier transform ion cyclotron resonance mass spectrometer. *Rapid Commun. Mass Spectrom.* **2008**, *22*, 3275−3285.
(7) Castaing, R.; Slodzian, G. Microanalyse par émission ionique secondaire. *J. Microsc. (Paris)* **1962**, *1*, 395.
(8) Slodzian, G. Etude d'une méthode d'analyse locale chimique et isotopique utilisant l'émission ionique secondaire. *Ann. Phys. (Paris, Fr.)* **1964**, *13*, 591−648.
(9) Castaing, R.; Slodzian, G. Analytical microscopy by secondary ion imaging techniques. *J. Phys. E: Sci. Instrum.* **1981**, *14*, 1119−1127.
(10) Schueler, B.; Sander, P.; Reed, D. A time-of-flight secondary ion microscope. *Vacuum* **1990**, *41*, 1661−1664.
(11) Luxembourg, S. L.; Mize, T. H.; McDonnell, L. A.; Heeren, R. M. A. High-spatial resolution mass spectrometric imaging of peptide and protein distributions on a surface. *Anal. Chem.* **2004**, *76*, 5339−5344.
(12) Llopart, X.; Ballabriga, R.; Campbell, M.; Tlustos, L.; Wong, W. Timepix, a 65k programmable pixel readout chip for arrival time, energy and/or photon counting measurements. *Nucl. Instrum. Methods Phys. Res., Sect. A* **2007**, *581*, 485−494.
(13) Jungmann, J. H.; MacAleese, L.; Buijs, R.; Giskes, F.; De Snaijer, A.; Visser, J.; Visschers, J.; Vrakking, M. J. J.; Heeren, R. M. A. Fast, high resolution mass spectrometry imaging using a medipix pixelated detector. *J. Am. Soc. Mass Spectrom.* **2010**, *21*, 2023−2030.
(14) Jungmann, J. H.; Gijsbertsen, A.; Visser, J.; Visschers, J.; Heeren, R. M. A.; Vrakking, M. J. J. A new imaging method for understanding chemical dynamics: Efficient slice imaging using an in-vacuum pixel detector. *Rev. Sci. Instrum.* **2010**, *81*, 103112.
(15) Brouard, M.; Johnsen, A. J.; Nomerotski, A.; Slater, C. S.; Vallance, C.; Yuen, W. H. Application of fast sensors to microscope mode spatial imaging mass spectrometry. *J. Instrum.* **2011**, *6*, C01044.
(16) Brouard, M.; Halford, E.; Lauer, A.; Slater, C. S.; Winter, B.; Yuen, W. H.; John, J. J.; Hill, L.; Nomerotski, A.; Clark, A.; Crooks, J.; Sedgwick, I.; Turchetta, R.; Lee, J. W. L.; Vallance, C.; Wilman, E. The application of the fast, multi-hit, pixel imaging mass spectrometry sensor to spatial imaging mass spectrometry. *Rev. Sci. Instrum.* **2012**, *83*, 114101.
(17) John, J. J.; Brouard, M.; Clark, A.; Crooks, J.; Halford, E.; Hill, L.; Lee, J. W. L.; Nomerotski, A.; Pisarczyk, R.; Sedgwick, I.; Slater, C. S.; Turchetta, R.; Vallance, C.; Wilman, E.; Winter, B.; Yuen, W. H. PImMS, a fast event-triggered monolithic pixel detector with storage of multiple timestamps. *J. Instrum.* **2012**, *7*, C08001.
(18) Kiss, A.; Jungmann, J. H.; Smith, D. F.; Heeren, R. M. Microscope mode secondary ion mass spectrometry imaging with a Timepix detector. *Rev. Sci. Instrum.* **2013**, *84*, 013704.
(19) Jungmann, J. H.; Smith, D. F.; Kiss, A.; MacAleese, L.; Buijs, R.; Heeren, R. M. A. An in-vacuum, pixelated detection system for mass spectrometric analysis and imaging of macromolecules. *Int. J. Mass Spectrom.* **2013**, *341*, 34−44.
(20) Kiss, A.; Smith, D. F.; Jungmann, J. H.; Heeren, R. M. A. Cluster secondary ion mass spectrometry microscope mode mass spectrometry imaging. *Rapid Commun. Mass Spectrom.* **2013**, *27*, 2745−2750.
(21) Halford, E.; Winter, B.; Mills, M. D.; Thompson, S. P.; Parr, V.; John, J. J.; Nomerotski, A.; Vallance, C.; Turchetta, R.; Brouard, M. Modifications to a commercially available linear mass spectrometer for mass-resolved microscopy with the pixel imaging mass spectrometry (PImMS) camera. *Rapid Commun. Mass Spectrom.* **2014**, *28*, 1649−1657.
(22) Vallance, C.; Brouard, M.; Lauer, A.; Slater, C. S.; Halford, E.; Winter, B.; King, S. J.; Lee, J. W. L.; Pooley, D. E.; Sedgwick, I.; Turchetta, R.; Nomerotski, A.; John, J. J.; Hill, L. Fast sensors for time-of-flight imaging applications. *Phys. Chem. Chem. Phys.* **2014**, *16*, 383−395.
(23) Wiley, W.; McLaren, I. H. Time-of-flight mass spectrometer with improved resolution. *Rev. Sci. Instrum.* **1955**, *26*, 1150−1157.
(24) Guilhaus, M.; Selby, D.; Mlynski, V. Orthogonal acceleration time-of-flight mass spectrometry. *Mass Spectrom. Rev.* **2000**, *19*, 65−107.
(25) Aoki, J.; Hazama, H.; Toyoda, M. Novel ion extraction method for imaging mass spectrometry. *J. Mass Spectrom. Soc. Jpn.* **2011**, *59*, 57−61.
(26) Suckau, D.; Resemann, A.; Schuerenberg, M.; Hufnagel, P.; Franzen, J.; Holle, A. A novel MALDI LIFT-TOF/TOF mass spectrometer for proteomics. *Anal. Bioanal. Chem.* **2003**, *376*, 952−965.
(27) Guo, A. Improving the performance of microscope mass spectrometry imaging. Ph.D. thesis, University of Oxford, 2018.
(28) Guo, A.; Burt, M.; Brouard, M. Mass-resolved ion microscope imaging over expanded mass ranges using double-field post-extraction differential acceleration. *Int. J. Mass Spectrom.* **2018**, *429*, 121−126.
(29) Kovtoun, S. V.; Cotter, R. J. Mass-correlated pulsed extraction: theoretical analysis and implementation with a linear matrix-assisted laser desorption/ionization time of flight mass spectrometer. *J. Am. Soc. Mass Spectrom.* **2000**, *11*, 841−853.
(30) Beavis, R. C.; Chait, B. T. Velocity distributions of intact high mass polypeptide molecule ions produced by matrix assisted laser desorption. *Chem. Phys. Lett.* **1991**, *181*, 479−484.
(31) Pan, Y.; Cotter, R. J. Measurement of initial translational energies of peptide ions in laser desorption/ionization mass spectrometry. *Org. Mass Spectrom.* **1992**, *27*, 3−8.
(32) Glückmann, M.; Karas, M. The initial ion velocity and its dependence on matrix, analyte and preparation method in ultraviolet matrix-assisted laser desorption/ionization. *J. Mass Spectrom.* **1999**, *34*, 467−477.
(33) Burleigh, R. J.; Guo, A.; Smith, N.; Green, A.; Thompson, S.; Burt, M.; Brouard, M. Microscope imaging mass spectrometry with a reflectron. *Rev. Sci. Instrum.* **2020**, *91*, 023306.
(34) Burleigh, R. Development of high-throughput imaging mass spectrometry. Ph.D. thesis, University of Oxford, 2019.
(35) Winter, B.; Halford, E.; Brouard, M. Velocity corrected ion extraction in microscope mode imaging mass spectrometry. *Int. J. Mass Spectrom.* **2013**, *356*, 14−23.
(36) Colliver, T. L.; Brummel, C. L.; Pacholski, M. L.; Swanek, F. D.; Ewing, A. G.; Winograd, N. Atomic and molecular imaging at the single-cell level with TOF-SIMS. *Anal. Chem.* **1997**, *69*, 2225−2231.
(37) Halford, E. Microscope-mode imaging mass spectrometry with the PImMS camera. Ph.D. thesis, University of Oxford, 2016.

https://dx.doi.org/10.1021/jasms.0c00167
J. Am. Soc. Mass Spectrom. 2020, 31, 1903−1909